

Target Classification for Integrated Sensing and Communication in Industrial Deployments

Luca Barbieri¹, Marcus Henninger¹, Paolo Tosi¹, Artjom Grudnitsky¹, Mattia Brambilla²,
Monica Nicoli², Silvio Mandelli¹

¹*Nokia Bell Labs, Stuttgart, Germany*, ²*Politecnico di Milano, Milan, Italy*

Abstract—Integrated Sensing and Communication (ISAC) systems enable cellular networks to jointly operate as communication technology and sense the environment. While opportunities and potential performance have been largely investigated in simulations, few experimental works have showcased Automatic Target Recognition (ATR) effectiveness in a real-world deployment based on cellular radio units. To bridge this gap, this paper presents an initial study investigating the feasibility of ATR for ISAC. Our ATR solution uses a Deep Learning (DL)-based detector to infer the target class directly from the radar images generated by the ISAC system. The DL detector is evaluated with experimental data from a ISAC testbed based on commercially available mmWave radio units in the ARENA 2036 industrial research campus located in Stuttgart, Germany. Experimental results demonstrate accurate classification performance, demonstrating the feasibility of ATR ISAC with cellular hardware in our setup. We finally provide insights about the open generalization challenges, that will fuel future work on the topic.

Index Terms—6G, ISAC, Automatic Target Recognition, Machine Learning, mmWave.

I. INTRODUCTION

Sixth Generation (6G) cellular networks are transforming the telecommunication industry, accommodating the ever increasing demand for higher data rates, ubiquitous connectivity and ultra high reliability information exchange. One technology set to revolutionize this landscape is Integrated Sensing and Communication (ISAC) [1], [2], whereby part of the communication resources is reused for sensing purposes, allowing Base Stations (BSs) to behave as radar devices. Compared with previous Fifth Generation (5G) networks, these radar-like functionalities enable new use cases and applications, such as smart manufacturing [3], vulnerable road user protection [4] and intrusion detection [5], where the BSs can assist with complementary information about the possible presence of targets in the environment, ultimately enhancing safety.

While the integration of ISAC functionalities into 6G networks provides clear advantages compared with legacy 5G solutions, target detection based on ISAC brings additional challenges related to the communication-sensing co-design. For instance, compared with traditional millimeter Wave (mmWave) radars, ISAC systems need to share communication and sensing resources limiting the usability of the resulting radar images [5], [6]. An example of this are unwanted

artifacts due to utilizing standardized 5G Time Division Duplexing (TDD) frame structures originally not designed for sensing purposes, impacting the final radar image quality. These hurdles prevent an accurate target identification, calling for dedicated solutions able to adapt to these phenomena and improve object recognition performances. This is often accomplished by relying on Machine Learning (ML) strategies thanks to their ability of learning complex relationships in a fully data-driven fashion.

Target detection, often referred in the radar jargon as Automatic Target Recognition (ATR), has been widely investigated in previous years, especially for mmWave radars (see e.g., [7] for a review). On the other hand, ATR based on ISAC systems has been explored only recently. For example, in [8] the authors develop a programmable ISAC platform relying on commercial 5G hardware and demonstrate the feasibility of ML-based ATR for concealed and non-concealed objects. Fall detection is investigated in [9] for ISAC-based Ultra WideBand (UWB) systems exploiting convolutional Neural Networks (NNs), while [10] focuses on Deep Learning (DL)-based gesture recognition relying on information extracted from 5G Synchronization Signal Blocks (SSBs). Other works instead concentrate on WiFi ISAC where the goal is to infer human activity via transformer-based NNs [11], to jointly carry out gesture recognition and human identification by means of 3D convolutional NNs [12] or to localize and count people [13], [14]. Even though previous works confirm the feasibility of ATR and similar recognition tasks, e.g. gesture, activity and human identification exploiting ISAC systems, there is a lack of works based on realistic cellular implementations. Thus, we aim to bridge this gap by investigating ATR in mmWave ISAC systems based on 5G commercial hardware.

In this paper, we aim to investigate the feasibility of ATR for cellular ISAC systems implemented on real-world hardware. Our study exploits DL-based strategies to infer the target class directly from the radar images generated by the ISAC solution. The goal is to provide an initial study highlighting key findings and takeaways that apply to cellular ISAC and demonstrate the possibilities of exploiting ISAC for object recognition tasks. To do so, we set up an extensive experimental campaign using a mmWave ISAC Proof of Concept (PoC) based on commercially-available 5G hardware deployed inside the ARENA 2036, an industrial research campus located in Stuttgart, Germany and considering different targets classes,

This work has received support from the European Commission through the ISLANDS project (grant agreement no. 101120544).

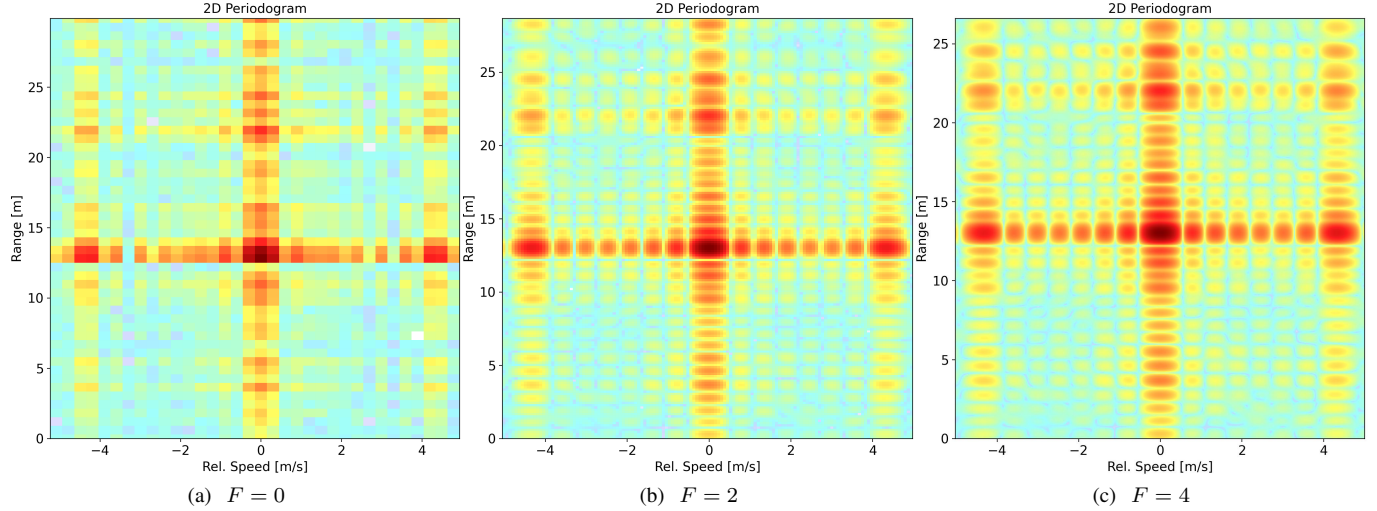


Fig. 1. Effect of different F values on the resulting periodogram \mathbf{P} containing a cabinet target: (a) $F = 0$, (b) $F = 2$, (c) $F = 4$.

ranging from small objects, i.e., corner reflectors, to large ones, e.g., forklifts. Experimental results show that integrating DL-based ATR solutions within cellular ISAC is promising. Indeed, we achieve an average accuracy of more than 99%, indicating that it is possible to infer the correct target class in almost all cases considered. Furthermore, we also shine light on generalizability issues that arise in DL-based ATR: horizontally flipping the radar images during testing considerably reduces the performances of the DL detector for some classes. Thus, proper countermeasures are needed to improve performances under unseen testing conditions. We leave this extension as a future research activity.

The rest of the paper is organized as follows: Sec. II introduces the ISAC PoC and the radar image generation process, while Sec. III presents the general architecture of the DL-based ATR detector used in the paper. Sec. IV describes the experimental activity done for performance assessment, whose results are analyzed in Sec. V. Finally, Sec. VI draws conclusions.

II. MMWAVE ISAC REAL-WORLD SETUP

This section details the real-world ISAC setup used for collecting the data. Sec. II-A presents the ISAC PoC together with the main parameters characterizing it, while Sec. II-B explains how the data extracted from the PoC is converted to a suitable radar image that can be used for ML-based ATR.

A. mmWave ISAC PoC

For our experiments, we rely on the ISAC PoC described in [15] with the main radio parameters summarized in Table I. This system is implemented using 5G commercial hardware operating in the Frequency Range 2 (FR2) with a central frequency of 27.4 GHz and consists of two radio devices: a half-duplex gNodeB (gNB) Radio Unit (RU) configured as the transmitter, and a sniffer RU acting as the receiver. Note that receiver and transmitter are physically separated but quasi co-located, meaning that the overall system can be regarded as a

mono-static sensing setup. As far as the actual communication parameters are concerned, the ISAC PoC exploits the 5G numerology $\mu = 3$ [16] with $N = 1584$ subcarriers with a spacing among them of 120 kHz and a total bandwidth of 190 MHz. The gNB RU transmits in downlink 5G-compliant Orthogonal Frequency Division Multiplexing (OFDM) radio frames with a duration of 10 ms using a TDD pattern that repeats every 1.25 ms. The TDD pattern accommodates for 104 and 36 symbols for downlink and uplink transmission, respectively, resulting in $M = 1120$ total symbols for each radio frame. On the other hand, the sniffer RU operates in uplink and it is synchronized with the gNB RU. Upon reception of the reflected signal by the sniffer RU, a dedicated server processes the IQ samples and computes the channel impulse response \mathbf{H} for each radio frame as discussed in the next section. Note that both gNB and sniffer RUs are configured to use the same fixed beam, with 14° half-power beam width (both in azimuth and elevation), for transmitting and receiving the radio signals, respectively. For any additional information on the ISAC PoC we refer the interested reader to [15].

B. Radar images generation

Let $\mathbf{X} \in \mathbb{C}^{N \times M}$ denote the transmitted OFDM frame by the gNB RU composed by M symbols and N subcarriers. Upon

TABLE I
ISAC PoC RADIO PARAMETERS

Parameter	Description	Value
f_c	Central frequency	27.4 GHz
B	Total bandwidth $N \cdot \Delta f$	190 MHz
N	Number of subcarriers	1584
M	Number of OFDM symbols per frame	1120
Δf	Subcarrier spacing	120 kHz
T_O	OFDM symbol time	8.33 μ s
T_{CP}	Cyclic Prefix (CP) length	0.59 μ s
T_s	OFDM symbol time including CP	8.92 μ s

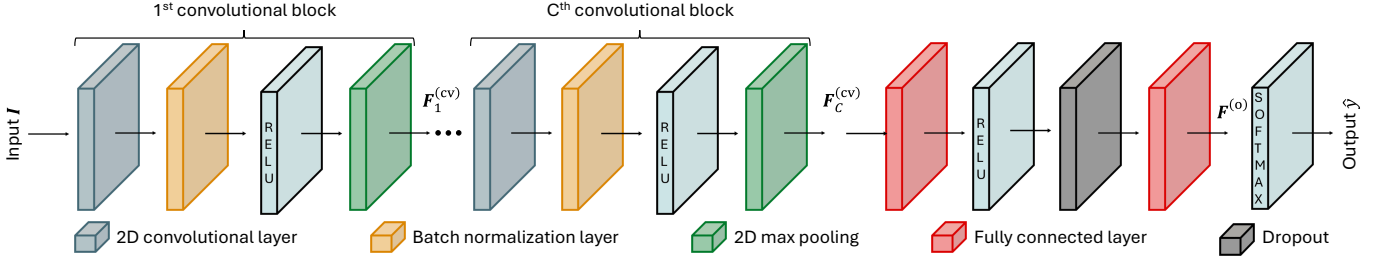


Fig. 2. Architecture for the convolutional-based ATR detector: the input is processed by a variable number of convolutional blocks to extract fine-grained features which are fed to two fully connected layers for estimating the final target class.

reception of the received signal $\mathbf{Y} \in \mathbb{C}^{N \times M}$ by the sniffer RU we can get an estimate of the channel matrix $\mathbf{H} \in \mathbb{C}^{N \times M}$ by element-wise division denoted as

$$\mathbf{H} = \mathbf{Y} \oslash \mathbf{X}, \quad (1)$$

which carries information about the number of possible targets inside the surrounding environment and their (rough) physical location. Given the estimated channel matrix \mathbf{H} , we compute the 2D periodogram over the Doppler/delay domain by first applying a Discrete Fourier Transform (DFT) on the OFDM symbols and then running an Inverse Discrete Fourier Transform (IDFT) over the subcarriers. Each element of the periodogram $\mathbf{P} \in \mathbb{C}^{N' \times M'}$ is expressed as [17]

$$\mathbf{P}_{n,m} = \frac{1}{M'N'} \sum_{k=0}^{N'} \left(\sum_{\ell=0}^{M'} \mathbf{H}_{k,\ell} e^{-j2\pi \frac{\ell m}{M'}} \right) e^{j2\pi \frac{kn}{N'}}, \quad (2)$$

where $N' = 2^{\lceil \log_2 N \rceil + F}$ and $M' = 2^{\lceil \log_2 M \rceil + F}$ are the number of rows and columns of \mathbf{H} after zero padding, while F is the padding factor, a design parameter used for controlling the granularity of the resulting periodogram. To get intuitive insights on the effect of different F choices on the generation of \mathbf{P} , please see Fig. 1. The delay-Doppler information in \mathbf{P} contains all the necessary details to carry out target detection.

III. DATA-DRIVEN ATR SYSTEM

The periodogram generated by the ISAC system is used to understand the presence of targets as well as their physical properties (e.g., discerning different object types). For this purpose, we rely on DL methodologies, namely convolutional NNs, to infer the type of target being observed by the ISAC system. Formally, given \mathbf{P} as input, the goal of the DL-based detector is to output the object type $y \in \mathcal{Y}$ among a set \mathcal{Y} of pre-defined target classes with $T = |\mathcal{Y}|$ being the number of possible target classes. In what follows, we break down the operations performed by the detector, whose general structure is highlighted in Fig. 2.

Starting from the complex periodograms, we concatenate magnitude and phase information from \mathbf{P} and feed it to the DL model such that each element of the input features $\mathbf{I} \in \mathbb{R}^{N' \times M' \times 2}$ is computed as follows

$$\mathbf{I}_{m,n} = [\|\mathbf{P}_{m,n}\|, \phi(\mathbf{P}_{m,n})]^T, \quad (3)$$

with $\phi(\cdot)$ denoting the phase extraction operation. Then, we have a variable number C of convolutional blocks whose goal is to extract fine-grained features to help the final classification. Each block is composed by a 2D convolutional layer followed by a batch normalization layer with a ReLU activation function and a 2D max pooling operation. Specifically, the output at the c -th block with $c = 1, \dots, C$ can be generally expressed as

$$\mathbf{F}_c^{(cv)} = g_{cv} \left(\mathbf{F}_{c-1}^{(cv)} \right), \quad (4)$$

where $\mathbf{F}_{c-1}^{(cv)}$ are the features of the $(c-1)$ -th block with $\mathbf{F}_{c-1}^{(cv)} = \mathbf{I}$ when $c = 1$, while $g_{cv}(\cdot)$ encapsulates the processing done by the convolutional block. After the C -th block, we feed $\mathbf{F}_C^{(cv)}$ to two fully connected layers with a dropout layer in between to get the final features $\mathbf{F}^{(o)}$ for classification. Specifically, the output of these layers is computed as

$$\mathbf{F}^{(o)} = g_{fc}^{(1)}(g_{fc}^{(2)}(\mathbf{F}_C^{(cv)})), \quad (5)$$

where $g_{fc}^{(1)}(\cdot)$ and $g_{fc}^{(2)}(\cdot)$ denote the processing performed by the first and second fully connected layers, respectively. The final class is then obtained via a softmax operation $g_{sf}(.)$ applied to the output of the last fully connected layer as

$$\hat{y} = g_{sf}(\mathbf{F}^{(o)}). \quad (6)$$

The DL model parameters are optimized by minimizing a weighted version of the cross entropy loss between the predicted label \hat{y} and the true one y for the samples in the training set. This is done to account for possible imbalances, i.e., number of training examples, across different target classes. Note that the final choice of the number of convolutional blocks C as well as the parameters characterizing all the layers of the detector is optimized as detailed in Sec. V.

IV. MEASUREMENT CAMPAIGN

To assess the ATR feasibility for cellular ISAC systems, we design an extensive experimental campaign aimed at evaluating the accuracy provided by the DL-based ATR detector in correctly classifying a wide variety of different target classes.

The measurement campaign has been carried out in the ARENA 2036 industrial research campus located in Stuttgart, Germany, where the ISAC PoC has been mounted at a height of 5.12 m to surveil an area in front of it. The area covers a maximum distance of 23 m, dictated by a wall with a cargo gate present at the end of the area, and is free from major

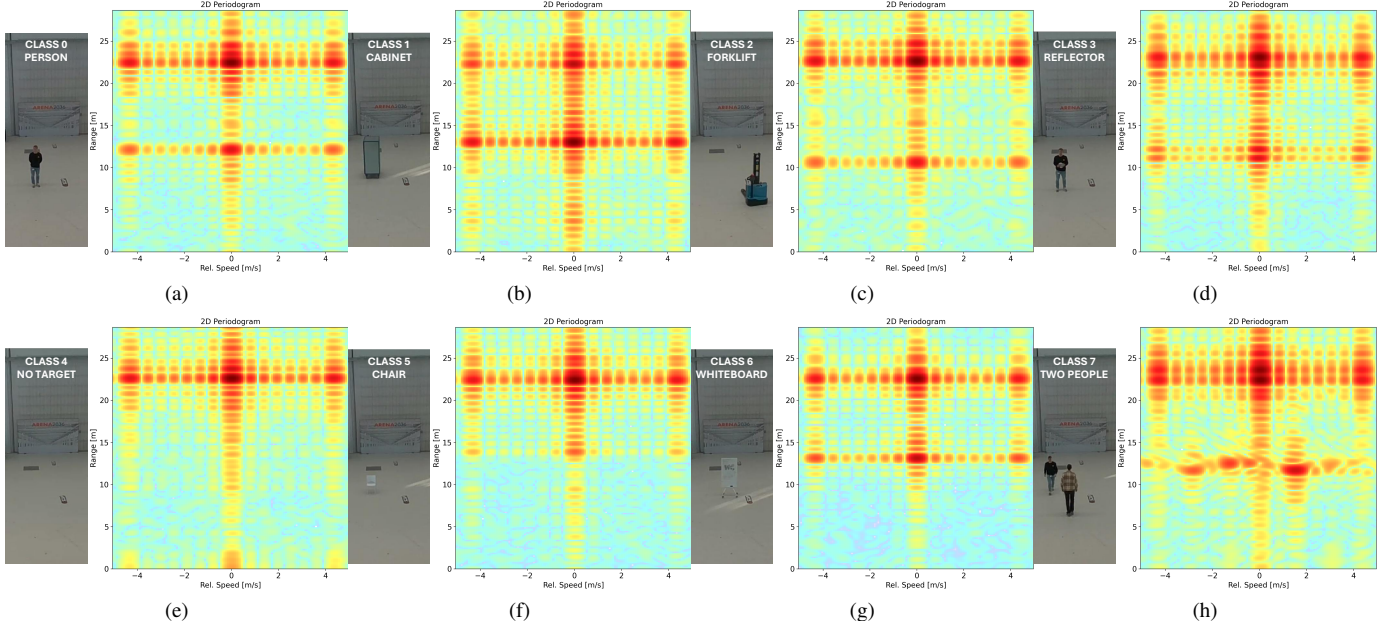


Fig. 3. Measurements collected during the experimental campaign. Each panel shows the periodogram, on the right, and the corresponding visual representation collected via a camera, on the left, for the targets: (a) person, (b) cabinet, (c) forklift, (d) reflector, (e) no target, (f) chair, (g) whiteboard and (h) two people.

obstructions, allowing us to capture the effect of each target on the resulting periodograms collected during the campaign. The experiments focus on collecting ISAC data to form a dataset for ML purposes. The following target classes and movements have been considered:

- Person (class 0): a person is placed at two different distances, approximately at 11 m and 18 m. Then, the person walks in a straight line moving away from the PoC and back. The same movement is then recorded when the person runs instead of walking.
- Cabinet (class 1): a large metallic cabinet structure is first placed at a fixed distance (roughly 15 m from the PoC). Then, we move the cabinet in a straight line following the same trajectory for class 0.
- Forklift (class 2): a small forklift is placed at a fixed distance of 11 m from the PoC.
- Reflector (class 3): a person carrying a small corner reflector is placed at 11 m and 18 m from the PoC. As done before, we record also the movement of the person walking/running away from the PoC and back.
- No target (class 4): in this case the area in front of the PoC does not contain any target of interest and is free from any obstruction.
- Chair (class 5): we place a white chair at a fixed distance of 15 m from the PoC.
- Whiteboard (class 6): similar for class 5, we place a whiteboard at a fixed distance of 15 m from the PoC.
- Two people (class 7): two people move in opposing motion. The first one starts near the PoC while the second begins close to the end of the area. The velocity of each person varies over time, with parts of the trajectory where they walk and parts of it where they run.

According to the above discussion, we strive to maximize diversity while collecting data by considering different distances as well as movement types (i.e., walking and running) for most of the targets considered. This allows us to benchmark the performances of the DL-based detector under conditions that are as general as possible and provide more comprehensive conclusions and takeaways. For each of the considered targets in the dataset, we show in Fig. 3 an exemplary periodogram with the associated target captured via a camera system. By comparing the different periodograms, some classes show quite similar visual properties that make them hardly distinguishable, calling for dedicated ML-based processing techniques. Finally, Table II highlights the number of periodograms collected for each class, the ratio of data per each class with respect to the total number of periodograms, as well as the number of train/test examples used for DL-based ATR training and testing.

TABLE II
MEASUREMENT CAMPAIGN STATISTICS

Class	Periodograms [#]	Ratio [%]	Train/test samples [#]
0	2564	19.58	2051/513
1	1635	12.48	1308/327
2	1051	8.03	841/210
3	3345	25.55	2776/569
4	1108	8.46	886/222
5	803	6.14	643/160
6	754	5.77	604/150
7	1832	13.99	1466/366
Total	13092	100	10575/2517

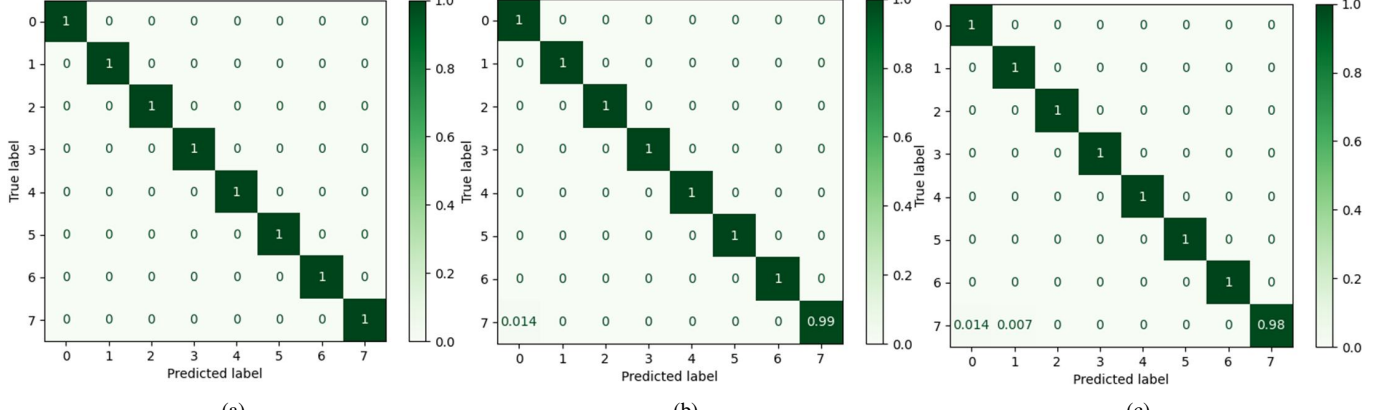


Fig. 4. Confusion matrices attained by the ATR detector for: (a) $F = 0$, (b) $F = 1$ and (c) $F = 2$. The average accuracy for $F = 0$, $F = 1$ and $F = 2$ is 99.96%, 99.91% and 99.91%, respectively.

V. EXPERIMENTAL RESULTS

This section details the experimental results provided by the DL-based ATR detector. We start by describing the optimization process used to find the best architecture in terms of layer choices as well as parameters characterizing each NN layer in Sec. V-A. Then, in Sec. V-B, we present the results provided by the optimized configuration of the detector, highlighting also possible generalization abilities.

A. NN optimization and best architecture search

We implement an architecture search on the NN model defined in Sec. III to optimize its structure, e.g., number of layers and their associated configuration parameters, according to the value of the padding factor F selected.

We optimize the number $C \in [2, 4]$ of convolutional blocks, while for the convolutional layers we search for the best kernel size $k_c \in [7, 5, 3]$, stride size $s_c \in [2, 1]$ and number of output channels $o_c \in [16, 8, 4]$. Similarly, we search for the optimal kernel size $k_m \in [2, 1]$ and stride size $s_m \in [2, 1]$ for the max pooling operations performed inside the convolutional blocks. We follow a widely adopted choice in the literature of doubling the number of channel outputs after every convolutional layer, see e.g., [18] and [19]. In our search o_c refers to the number of output channels of the first layer, while subsequent layers adopt multiple of 2s for the number of output channels. As an example of this strategy, if $C = 4$ and $o_c = 4$, the first convolutional layer has 4 output channels, the second 8, the third 16 and the last one 32. Additionally, we fix k_c only of the first convolutional layer according to the F value selected, namely if $F = 0$, $F = 1$ and $F = 2$ we select $k_c = 3$, $k_c = 5$ and $k_c = 7$, respectively. Finally, for what concerns the fully connected layers, we search for the best number of output features $f \in [16, 32, 64]$, while also optimizing the dropout rate d with $d \in [0.8, 0.5]$. All other parameters are fixed, namely we choose a batch size of 32 examples, adopt the SGD optimizer with a learning rate of 0.001 and a number of epochs for training of 50 without any learning rate scheduler.

The best architectural design of the DL-based ATR detector is done by randomly configuring the NN with the parameters defined above and monitoring the testing loss at the end of the training process. We make 80 different configurations for each of the F values selected, namely $F = 0$, $F = 1$ and $F = 2$, and choose the resulting architecture giving the lowest testing loss for each one of them. This process provides at the output the NN architectures whose configurations parameters are defined in Table III together with their number D of trainable parameters. Overall, smaller padding factors (i.e., $F = 0$ or $F = 1$) call for a lower number of convolutional blocks for maximizing the performances, while for larger ones (i.e., $F = 2$) one should adopt more convolutional blocks. This is reasonable as F controls the granularity of the periodograms: increasing F leads to more fine-grain details in \mathbf{P} ultimately requiring more convolutional layers to process them and fully exploit for the final classification.

B. ATR accuracy and generalization capabilities

As a first set of results, we present the classification accuracy attained by the DL-based ATR detector over the different values of the padding factor F . Specifically, Fig. 4 shows the confusion matrices that highlight the accuracy for each target class individually considering $F = 0$ (Fig. 4a), $F = 1$ (Fig. 4b) and $F = 2$ (Fig. 4c). The results show that the performances

TABLE III
OPTIMIZED ARCHITECTURES FOR THE CHOSEN VALUES OF F

$F = 0$		$F = 1$		$F = 2$	
Parameter	Value	Parameter	Value	Parameter	Value
C	2	C	2	C	4
k_c	3	k_c	3	k_c	3
s_c	1	s_c	1	s_c	1
o_c	16	o_c	16	o_c	8
k_m	2	k_m	2	k_m	2
s_m	2	s_m	2	s_m	2
f	32	f	32	f	32
d	0.5	d	0.5	d	0.5
D	178k	D	343k	D	136k

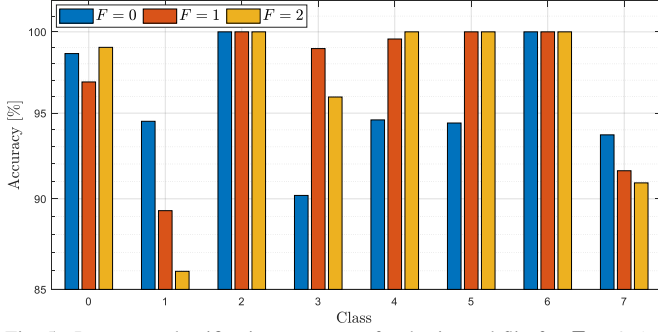


Fig. 5. Per-target classification accuracy after horizontal flip for $F = 0, 1, 2$.

attained by the ATR detector are not influenced much by the padding factor selected. Indeed, the average accuracy attained across the F values is nearly identical, apart from minor differences for the last target class, i.e., the two people case. The results thus suggest that exploiting DL methodologies for ATR from ISAC system is highly effective as it provides excellent recognition abilities.

We also evaluate the generalizability of the trained DL detectors by horizontally shifting all periodogram samples contained in the testing dataset and evaluating its effects on the final classification accuracy. Conceptually, this processing does not affect the appearance of the targets or their distance from the ISAC PoC but merely flips the relative velocity information. This makes targets moving in a specific direction appear to be moving in the opposite. Fig. 5 shows the results of the procedure, highlighting the accuracy per target class attained by the DL detectors over the different values of F . Comparing the results, selecting a single F parameter might not be feasible as there is no value guaranteeing the highest performance across all target classes. The analysis also suggests that DL methods for ATR could benefit from augmentation strategies or dedicated countermeasures to improve performances in unseen scenarios. Indeed, under all F values, the accuracy for some target classes, i.e., person and two people classes, diminishes quite considerably. Conventional augmentation strategies currently developed for images do not reflect well the complex interactions captured by the communication channel, calling for ad-hoc augmentations that provide physically plausible transformations to the targets being currently detected by the ISAC system. We leave this problem for future works.

VI. CONCLUSIONS

In this paper we investigated the feasibility of conducting ATR fully relying on cellular ISAC systems implemented over real-world 5G mmWave hardware. We conducted an extensive experimental campaign comprising 8 different target classes together with varying movement patterns. Based on the collected data from the ISAC PoC, we optimized a DL-based ATR detector in terms of architectural choices to maximize its classification accuracy over varying padding factors that rule the granularity of the gathered radar images. Experimental results show the feasibility of exploiting DL methodologies

for ISAC ATR as they are able to correctly recognize all target classes in nearly all conditions considered. Nevertheless, introducing data augmentation (i.e., horizontally flipping the periodograms) during testing substantially reduces classification accuracy for some target classes. This highlights the need for a generalizable ATR solution able to adapt to different sensing operations, environments and unseen conditions. We strive to tackle this problem in future works by extending this preliminary study to more complex scenarios by considering a wider range of possible targets and movement combinations, as well as explore dedicated strategies to deal with changing environments and ISAC PoC parameters configuration, without requiring a full re-training of the DL-based ATR solutions.

REFERENCES

- [1] Z. Wei, H. Qu, Y. Wang *et al.*, “Integrated sensing and communication signals toward 5G-A and 6G: A survey,” *IEEE Internet of Things Journal*, vol. 10, no. 13, pp. 11068–11092, 2023.
- [2] S. Mandelli, M. Henninger, M. Bauhofer *et al.*, “Survey on integrated sensing and communication performance modeling and use cases feasibility,” in *2023 2nd International Conference on 6G Networking (6GNet)*, 2023, pp. 1–8.
- [3] X. Zhu, J. Liu, L. Lu *et al.*, “Enabling intelligent connectivity: A survey of secure ISAC in 6G networks,” *IEEE Communications Surveys & Tutorials*, pp. 748–781, 2024.
- [4] X. Cheng, D. Duan, S. Gao *et al.*, “Integrated sensing and communications (ISAC) for vehicular communication networks (VCN),” *IEEE Internet of Things Journal*, vol. 9, no. 23, pp. 23 441–23 451, 2022.
- [5] P. Tosi, M. Henninger, L. G. de Oliveira *et al.*, “Feasibility of non-line-of-sight integrated sensing and communication at mmWave,” in *2024 IEEE 25th International Workshop on Signal Processing Advances in Wireless Communications (SPAWC)*, 2024, pp. 331–335.
- [6] M. Henninger, L. G. de Oliveira, S. Saur *et al.*, “Target detection for ISAC with TDD transmission,” *arXiv e-prints*, 2025. [Online]. Available: <https://arxiv.org/abs/2504.19260>
- [7] Z. Geng, H. Yan, J. Zhang *et al.*, “Deep-learning for radar: A survey,” *IEEE Access*, vol. 9, pp. 141 800–141 818, 2021.
- [8] A. Paidimari, A. Tzadok, S. Garcia Sanchez *et al.*, “Eye-beam: A mmwave 5G-compliant platform for integrated communications and sensing enabling AI-based object recognition,” *IEEE Journal on Selected Areas in Communications*, vol. 42, no. 9, pp. 2354–2368, 2024.
- [9] A. Li, E. Bodanese, S. Poslad *et al.*, “An integrated sensing and communication system for fall detection and recognition using ultrawideband signals,” *IEEE Internet of Things Journal*, vol. 11, no. 1, pp. 1509–1521, 2024.
- [10] M. Dwivedi, I. E. L. Hulede, O. Venegas *et al.*, “5G-based passive radar sensing for human activity recognition using deep learning,” in *2024 IEEE Radar Conference (RadarConf24)*, 2024, pp. 1–6.
- [11] F. Luo, S. Khan, B. Jiang *et al.*, “Vision transformers for human activity recognition using WiFi channel state information,” *IEEE Internet of Things Journal*, vol. 11, no. 17, pp. 28 111–28 122, 2024.
- [12] R. Zhang, C. Jiang, S. Wu *et al.*, “Wi-Fi sensing for joint gesture recognition and human identification from few samples in human-computer interaction,” *IEEE Journal on Selected Areas in Communications*, vol. 40, no. 7, pp. 2193–2205, 2022.
- [13] S. Kianoush, S. Savazzi, V. Rampa *et al.*, “People counting by dense WiFi MIMO networks: Channel features and machine learning algorithms,” *Sensors*, vol. 19, no. 16, 2019. [Online]. Available: <https://www.mdpi.com/1424-8220/19/16/3450>
- [14] S. Savazzi, S. Sigg, M. Nicoli *et al.*, “Device-free radio vision for assisted living: Leveraging wireless channel quality information for human sensing,” *IEEE Signal Processing Magazine*, vol. 33, no. 2, pp. 45–58, 2016.
- [15] T. Wild, A. Grudnitsky, S. Mandelli *et al.*, “6G integrated sensing and communication: From vision to realization,” in *2023 20th European Radar Conference (EuRAD)*, 2023, pp. 355–358.
- [16] 3GPP TS 38.221 V19.0.0, “3rd generation partnership project; technical specification group radio access networks; NR; physical channels and modulations; stage 2 (Release 19),” 2025.

- [17] K. M. Braun, "OFDM radar algorithms in mobile communication networks," Ph.D. dissertation, Karlsruher Institut für Technologie (KIT), 2014.
- [18] K. Simonyan and A. Zisserman, "Very deep convolutional networks for large-scale image recognition," in *3rd International Conference on Learning Representations, ICLR 2015*, 2015.
- [19] K. He, X. Zhang, S. Ren *et al.*, "Deep residual learning for image recognition," in *2016 IEEE Conference on Computer Vision and Pattern Recognition (CVPR)*, 2016, pp. 770–778.